Journal of Structural Biology 195 (2016) 337–344

Contents lists available at ScienceDirect

Journal of Structural Biology

journal homepage: www.elsevier.com/locate/yjsbi

Bone mineral crystal size and organization vary across mature rat bone cortex

Mikael J. Turunen [a,b,*], Jørn D. Kaspersen [a], Ulf Olsson [c], Manuel Guizar-Sicairos [d], Martin Bech [e], Florian Schaff [f], Magnus Tägil [g], Jukka S. Jurvelin [b,h], Hanna Isaksson [a,g]

[a] Department of Biomedical Engineering, Lund University, Lund, Sweden
[b] Department of Applied Physics, University of Eastern Finland, Kuopio, Finland
[c] Division of Physical Chemistry, Lund University, Lund, Sweden
[d] Paul Scherrer Institut, Villigen PSI, Villigen, Switzerland
[e] Department for Medical Radiation Physics, Lund University, Lund, Sweden
[f] Physik-Department und Institut für Medizintechnik, Technische Universität München, Garching, Germany
[g] Department of Orthopaedics, Clinical Sciences, Lund University, Lund, Sweden
[h] Diagnostic Imaging Centre, Kuopio University Hospital, Kuopio, Finland

ARTICLE INFO

Article history:
Received 13 April 2016
Received in revised form 7 July 2016
Accepted 9 July 2016
Available online 11 July 2016

Keywords:
Bone mineralization
Rat
Osteoporosis
Small/wide angle X-ray scattering
Fourier transform infrared spectroscopy

ABSTRACT

The macro- and micro-features of bone can be assessed by using imaging methods. However, nano- and molecular features require more detailed characterization, such as use of *e.g.*, vibrational spectroscopy and X-ray scattering. Nano- and molecular features also affect the mechanical competence of bone tissue. The aim of the present study was to reveal the effects of mineralization and its alterations on the mineral crystal scale, by investigating the spatial variation of molecular composition and mineral crystal structure across the cross-section of femur diaphyses in young rats, and healthy and osteoporotic mature rats ($N = 5$). Fourier transform infrared spectroscopy and scanning small- and wide-angle X-ray scattering (SAXS/WAXS) techniques with high spatial resolution were used at identical locations over the whole cross-section. This allowed quantification of point-by-point information about the spatial distribution of mineral crystal volume. All measured parameters (crystal dimensions, degree of orientation and predominant orientation) varied across the cortex. Specifically, the crystal dimensions were lower in the central cortex than in the endosteal and periosteal regions. Mineral crystal orientation followed the cortical circumference in the periosteal and endosteal regions, but was less well-oriented in the central regions. Central cortex is formed rapidly during development through endochondral ossification. Since rats possess no osteonal remodeling, this bone remains (until old age). Significant linear correlations were observed between the dimensional and organizational parameters, *e.g.*, between crystal length and degree of orientation ($R^2 = 0.83$, $p < 0.001$). Application of SAXS/WAXS provides valuable information on bone nanostructure and its constituents, effects of diseases and, prospectively, mechanical competence.

1. Introduction

Bone structure, composition, and shape change continuously due to bone formation and resorption. While the macro- and microscale properties of bone can be assessed by using different imaging methods, *e.g.*, X-ray computed tomography, information on the molecular- and nanolevel characteristics require a different approach. Vibrational spectroscopy and X-ray scattering methods can be used (Boskey and Pleshko Camacho, 2007; Bunger et al., 2010; Fratzl et al., 1996a,b; Mathavan et al., 2015; Turunen et al., 2014, 2011). The organization and structure of bone on all length scales (including the nanoscale) contribute to the mechanical competence of bone, and alterations may result in *e.g.* an increased fracture risk as a result of osteoporosis. Efforts have been made to understand and determine the collagen and mineral crystal structure, content, and organization in bone (Acerbo et al., 2014; Bunger et al., 2010, 2006; Camacho et al., 1999; Fratzl et al.,

* Corresponding author at: Department of Applied Physics, University of Eastern Finland, POB 1627, FI-70211, Kuopio, Finland.
E-mail addresses: mikael.turunen@uef.fi (M.J. Turunen), dovling@gmail.com (J.D. Kaspersen), ulf.olsson@fkem1.lu.se (U. Olsson), manuel.guizar-sicairos@psi.ch (M. Guizar-Sicairos), martin.bech@med.lu.se (M. Bech), florian.schaff@tum.de (F. Schaff), magnus.tagil@med.lu.se (M. Tägil), jukka.jurvelin@uef.fi (J.S. Jurvelin), hanna.isaksson@bme.lth.se (H. Isaksson).

http://dx.doi.org/10.1016/j.jsb.2016.07.005
1047-8477/

1992; Giannini et al., 2014; Turunen et al., 2014). However, the effects of alterations in mineralization, *e.g.*, due to osteoporosis and variation in tissue formation mechanisms, on mineral crystal size and organization remain unclear.

Hydroxyapatite (HA) crystals and collagen fibers are the basic building blocks of bone. The HA crystals are a few hundred angstrom long and wide and about 20–40 Å thick (Bunger et al., 2010; Camacho et al., 1999; Weiner and Traub, 1992). With the collagen fibers they form a three-dimensional framework in which the crystal plates grow in relatively parallel layers (Weiner and Traub, 1992). The mineral plates are organized within the collagen fibrils (Weiner et al., 1991) but mineralization also occurs on the fibril surface (Landis et al., 1996). The mineral crystals are arranged tightly together (Schwarcz et al., 2014) and their preferred orientation, together with the collagen fibrils, follows the primary direction of mechanical loading, *i.e.*, along the direction of the shaft in a long bone. Arrays of these mineralized collagen fibers form lamellae, which in cortical bone are formed as a result of Haversian modeling and remodeling, the formation of osteons, or as a result of periosteal and endosteal remodeling. To directly visualize these basic building blocks, the mineral crystals, transmission electron microscopy is needed (Weiner and Traub, 1992).

Rodent bones do not undergo Haversian remodeling, and thus possess no osteons. The exact reason is unknown, but instead of Haversian remodeling, the bone formation and resorption occur on the periosteal and endosteal surfaces, resulting in circumferential lamellar bone (Bach-Gansmo et al., 2015, 2013; Shipov et al., 2013; Weiner and Traub, 1992; Weiner et al., 1991). The central bone has recently been shown to be more disorganized and to contain islands of remaining mineralized cartilage from the endochondral bone formation process (Bunger et al., 2010; Bach-Gansmo et al., 2015, 2013; Shipov et al., 2013). Thus, the oldest bone in rodent bone cortex is found in the central region. To some extent, rodent bones provide a simpler system to study mineralization. Indeed, the different regions across the bone may be representative of tissue that has been mineralized at different times. The effects of metabolic bone diseases, *e.g.*, osteoporosis, on local mechanisms of mineralization (mineral crystal size) are not well known (Donnelly et al., 2010). The ovariectomized (OVX) rat model of postmenopausal osteoporosis is well established for the assessment of effects of osteoporosis (Bagi et al., 1997; Kalu, 1991).

Small-angle X-ray scattering (SAXS) has been used to study the mineral properties in bone, including crystal thickness and orientation (Bunger et al., 2010; Fratzl et al., 1996a,b; Rinnerthaler et al., 1999). Recently we studied mineralization during bone healing in a rat femoral fracture model using SAXS (Turunen et al., 2014). In another study we investigated the mineral plate thicknesses in lumbar vertebra and proximal tibia of healthy and osteoporotic (OVX) rats (Mathavan et al., 2015). Other researchers have used combined small- and wide-angle X-ray scattering (SAXS/WAXS) (Acerbo et al., 2014; Giannini et al., 2014) to investigate the nanometer-scale mineral crystal dimensions and orientations. They demonstrated decreased crystal length in the periosteal region of OVX rats (Acerbo et al., 2014). Moreover, the crystal length was lower in the periosteal region than in intracortical region but no differences in degree of orientation between intracortical and periosteal or control and OVX samples were observed. Giannini et al. showed that the long crystal direction [002] is aligned with the collagen fibers, whereas the collagen crystal direction [210] (width of the crystal) is perpendicular to [002] (Giannini et al., 2014). However, crystal dimensions were not determined.

The use of a narrow X-ray pencil beam with high flux, as available at synchrotron facilities, coupled with an automated scanning stage provides an opportunity to collect point-by-point matched SAXS and WAXS scattering data at high spatial resolution. The combined point-by-point SAXS and WAXS data enables the spatial quantification of all three mineral crystal dimensions, and consequently calculation of mineral crystal volume. This has not been determined earlier. Furthermore, as Fourier transform infrared (FTIR) spectroscopy can resolve the spatial distribution of the molecular composition of the tissue (Camacho et al., 1999; Turunen et al., 2014), combining SAXS and WAXS with FTIR data can provide a broad and detailed characterization of structure and composition of the bone on the nano- and molecular scale.

The aim of the present study was to investigate the spatial variation of molecular composition and mineral crystal structure over the cross-section of rat femur diaphyses. Mineral crystal dimensions, organization, mineralization (based on SAXS and WAXS), and molecular composition (based on FTIR spectroscopy) were compared and cross-correlated point-by-point and between regions of the bone cortex, *i.e.*, the periosteal region, the central region, and the endosteal region. Additionally, young and mature rats, as well as healthy and OVX rats were compared qualitatively.

2. Materials and methods

Cortical bone of five female Sprague-Dawley rat femora were harvested for SAXS, WAXS, and FTIR analyses. One rat was sacrificed at 10 weeks of age (referred to as "young"). At 12 weeks of age, two rats were ovariectomized (OVX) and two rats were kept as controls. The OVX and control rats were sacrificed at 30 weeks of age (referred to as "mature healthy" and "mature OVX"). The animal ethics and scientific advisory committee approved the care and experimental protocol (Ethical Permission No. M216-08, Lund University).

2.1. SAXS and WAXS

The left femora were harvested and the proximal half was embedded in epoxy resin. From each diaphysis of the proximal femur, 100 μm thick cross-sections were sawed using a low-speed, water-cooled IsoMet 11-1180 saw (Buehler, Illinois) with a diamond blade. SAXS and WAXS measurements were conducted at the cSAXS beamline at Swiss Light Source (SLS), Paul Scherrer Institut (PSI) in Villigen, Switzerland following outlined procedures (Bunk et al., 2009). Whole cortical bone cross-sections were raster-scanned with 20×20 μm^2 spot size and with scanning steps (pixel size) of 20 μm in a continuous line-scan mode. To cover the whole cortex the average area of acquisition was 4.3×4.0 mm. An exposure time of 50 ms and X-ray wavelength of 1.0 Å were used. The distance between the exit window and the sample was 25 cm (Fig. 1). For WAXS and SAXS the sample-detector distances were 30.8 cm and 711.9 cm providing q ranges of ~0.4–29.4 nm^{-1} and ~0.02–1.45 nm^{-1}, respectively (Fig. 1). For WAXS measurements an aperture of 1 mm was added 6 cm before the sample to reduce air-scattering. The distances to the detector were calibrated using a Silver-Behenate (AgBH) powder standard and the data were background corrected by subtracting air-background measurements. The beam center for SAXS was determined from the AgBH scattering pattern and from an actual bone measurement for WAXS. Between the SAXS and WAXS measurements, the setup was changed only by moving the detector but keeping the samples in place.

The SAXS and WAXS scattering patterns recorded with a Pilatus 2 M (Henrich et al., 2009) were azimuthally integrated in order to obtain $I(q)$ scattering curves (Fig. 1). The azimuthal integration was performed using only pixels with valid measurements, thereby excluding the pixels blocked by the beam stop, dead or hot pixels and insensitive gaps between the detector modules. The intensities in each pixel were corrected using geometrical and polarization

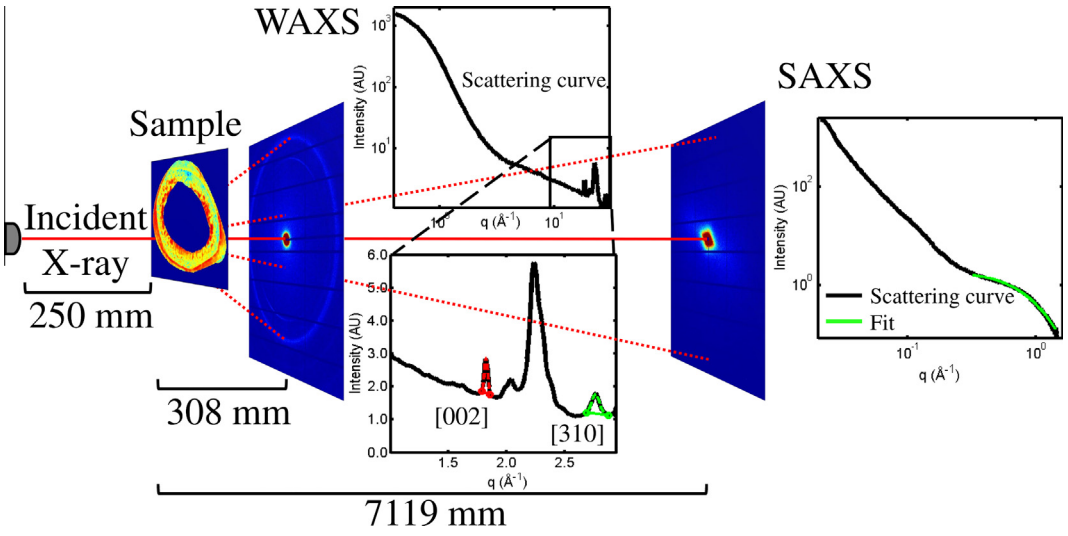

Fig. 1. Schematic presentation of the measurement setup showing the detector scattering images in WAXS and SAXS setup. The sample-detector distances for WAXS and SAXS were 30.8 cm and 711.9 cm, respectively. Also azimuthally integrated $I(q)$ scattering curves of WAXS and SAXS detector images are shown. Additionally, a typical fit to a SAXS scattering curve is shown as well as Gaussian-Lorenzian curves fitted to the [002] and [310] peaks of the WAXS curve.

correction factors (Pauw, 2014) which were especially prominent in WAXS.

To evaluate the mineral crystal lengths and widths from WAXS curves across the cortex cross-section the crystal lengths along the *c*-axis were determined from the width of the [002] reflection at Δq ~1.78–1.88 nm^{-1} (Fig. 1) (Acerbo et al., 2014; Lange et al., 2011). The widths in the *ab*-plane were derived from the [310] reflection (perpendicular to [002]) at Δq ~2.63–2.89 nm^{-1} (Acerbo et al., 2014; Lange et al., 2011). The exact locations of the peaks were determined using the second derivative of the scattering curve. To each peak, a Gaussian-Lorentzian curve with a scale parameter was fitted (Fig. 1). Subsequently, the full width at half maximum (FWHM) of the normalized fitted peak (without the scaling parameter) was used to calculate the crystal dimensions using Scherrer's equation:

$$D = \frac{K\lambda}{\beta_{1/2}\cos(\theta)},$$

where D is the average crystal size corresponding to the reflection, K is a constant describing the crystal shape (typically around 0.9), λ the X-ray wavelength, $\beta_{½}$ is the FWHM of the peak and θ is the scattering angle. The resolution broadening due to the instrument was considered negligible (10 times smaller than the detector pixel size) and was thus not implemented in the Scherrer's equation.

To determine the mineral crystal thickness the predominant orientation and the degree of orientation of the crystals in the cortex cross-section, from SAXS curves, the orientational parameters were obtained by fitting a Gaussian curve to the two symmetrical peaks of the azimuthal dependence $I(\psi)$. The predominant orientation and degree of orientation of the crystals were calculated from these Gaussian curves as described previously (Rinnerthaler et al., 1999). The mean crystal thickness was evaluated from SAXS curves using weighted iterative curve fitting to the $I(q)$ scattering curve (Fig. 1) as described earlier (Bunger et al., 2010). Briefly, in the model scattering is assumed to take place from a plate with finite thickness and infinite size in the other directions. The plate scattering is orientationally averaged with equal weight to all orientations, and the internal variation in mineral plate thicknesses is assumed to follow a Schulz-Zimm distribution. Furthermore, since two crystals cannot occupy the same volume, this excluded volume effect is perceived using the random phase approximation (RPA). In the present model, the low-q region in the $I(q)$ curve was excluded from the fitting. Thus, the effective structure factor, which describes the fluctuations at low q-values (Bunger et al., 2010), was not optimized in the fitting routine. The background term was added to the fit according to the study by Bunger et al. (2010). The initial guess for the background term was evaluated from the Porod-region where $I(q) \sim Pq^{-4}$ according to Porod's law (Glatter and Kratky, 1982). Thus, the total intensity of the fitted model (at q-range of 0.32–1.40 q^{-1}) was given by

$$I(q) = P_{eff}(q) + B,$$

where $P_{eff}(q)$ is the effective plate scattering including the RPA correction factor (Shimada et al., 1988) and B is the background term.

By assuming that the mineral crystals are plate-like, the crystal volume was calculated by multiplying the crystal thickness (curve fitting, SAXS) with the crystal length (peak [002], WAXS) and crystal width (peak [310], WAXS).

2.2. FTIR

For Fourier transform infrared (FTIR) microspectroscopy, three µm thick sections were cut sequential to those used for SAXS and WAXS using a HM 355S microtome (Thermo Scientific, MA, USA). The sections were placed on infrared transparent BaF_2 windows. FTIR measurements were conducted at the D7 beamline at the MAX-IV laboratory (Lund, Sweden). A Bruker 66V FTIR spectrometer (Bruker Corp., MA, USA) was coupled to a Bruker Hyperion 3000 IR microscope using a focal plane array (FPA) detector. Samples were measured with spectral resolution of 4 cm^{-1} and 64 scans were repeated for a wavelength range of 2000–800 cm^{-1}. The full femoral cortex cross-sections were imaged using the FPA detector (each array covers 128 × 128 elements corresponding to 340 × 340 µm^2) with binning of 4-by-4 to reduce the data set. Additionally, one region of only epoxy resin was measured. The average epoxy resin spectrum was normalized using the characteristic peak at 1728 cm^{-1} and subsequently subtracted from the bone spectra (Gadeleta et al., 2000; Isaksson et al., 2010; Rieppo et al., 2004). For each measurement point, the mineral/matrix ratio (M/M, 1200-900/1720-1585 cm^{-1}) to estimate the degree of mineralization (Boskey and Pleshko Camacho, 2007), crystallinity (1030/1020 cm^{-1}) to estimate the mineral crystal size and perfection (Durchschlag et al., 2006; Marcott et al., 1998), collagen

cross-linking ratio (XLR, 1660/1690 cm^{-1}) to estimate the collagen maturity (Courtland et al., 2008; Paschalis et al., 2001), and acid phosphate substitution (APS, 1127/1096 cm^{-1}) to indicate new bone formation (Spevak et al., 2013), were determined.

2.3. Spatial analysis

SAXS and WAXS analyses provided parameter maps from which the spatial distribution could be evaluated. Each cortex cross-section was divided into three areas representing the endosteal, central, and periosteal regions (Fig. 2). Since the central region contained more disorganized bone compared to the surrounding lamellar bone at endosteal and periosteal regions (Bach-Gansmo et al., 2013; Bunger et al., 2010; Shipov et al., 2013), the regional thicknesses were determined based on the maps of the predominant orientation (Fig. 2A) and then compared to the other SAXS/WAXS maps. Relative areas of the regions were determined by dividing the area of the region with the full cortex area (Fig. 2B). The average values of each region were calculated for each parameter and animal. The average results of each region from the two mature healthy and the two mature OVX samples were compared. The molecular composition maps from FTIR analyses were more homogeneous across the cortex and, therefore, determination of the region was not possible using the same criteria. Thus, molecular composition was evaluated for the whole cortex. All analyses were performed using custom-written scripts in MATLAB (R2012b, The MathWorks, Inc., MA).

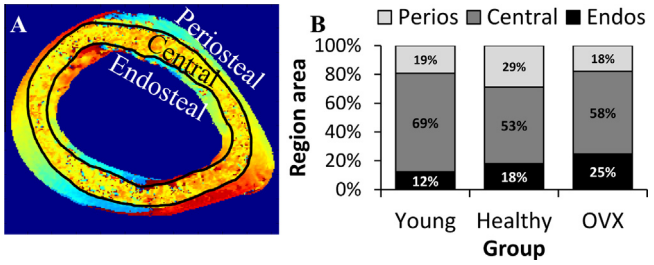

Fig. 2. Endosteal, central, and periosteal regions of bone cortex determined based on the predominant orientation map (A) and double-checked using other SAXS and WAXS maps. The division is based on the disorganized nature of bone in the central region (Bach-Gansmo et al., 2015, 2013). Relative areas (%) of endosteal, central, and periosteal regions in young (Young), mature healthy (Healthy), and mature OVX (OVX) samples are shown (B).

2.4. Statistical analysis

Spatial averages of each parameter from SAXS/WAXS analysis for endosteal, central, and periosteal regions of bone cortex (Fig. 2A) of mature rats (healthy and OVX) were compared using non-parametric Mann-Whitney *U*-test. Pearson's correlations between different parameters were determined using the spatial averages of the regions of each sample (SAXS/WAXS, 15 values) and for spatial averages of the whole cortex in each sample (FTIR, 5 values). Additionally, Pearson's correlations of point-by-point SAXS and WAXS data maps downscaled by a factor of four were calculated for all data-points of the five samples after merging the maps. Mann-Whitney *U*-test and Pearson's correlation analyses between the spatial averages was done using IBM SPSS statistics (v21, IBM corp., Armonk, NY). Pearson's correlations for point-by-point data maps were calculated using MATLAB. For all analyses, $p < 0.05$ was considered significant.

3. Results

All SAXS and WAXS parameter maps indicated visually a layered cortex structure, *i.e.*, endosteal, central, and periosteal regions (Fig. 2 and Fig. 3). However, the relative areas of these regions seemed to be different between young, healthy mature and OVX groups (Fig. 2B). The central region was thickest in the young sample whereas periosteal and endosteal regions were thicker in the healthy mature and OVX samples, respectively. Generally, all crystal dimensions showed lower values in the central cortex than in the endosteal and periosteal regions (Fig. 3A–D). Predominant orientation of the crystals in the cross-section of the cortex followed the cortical circumference in the endosteal and periosteal regions, while it was more random in the central region (Fig. 3E). This

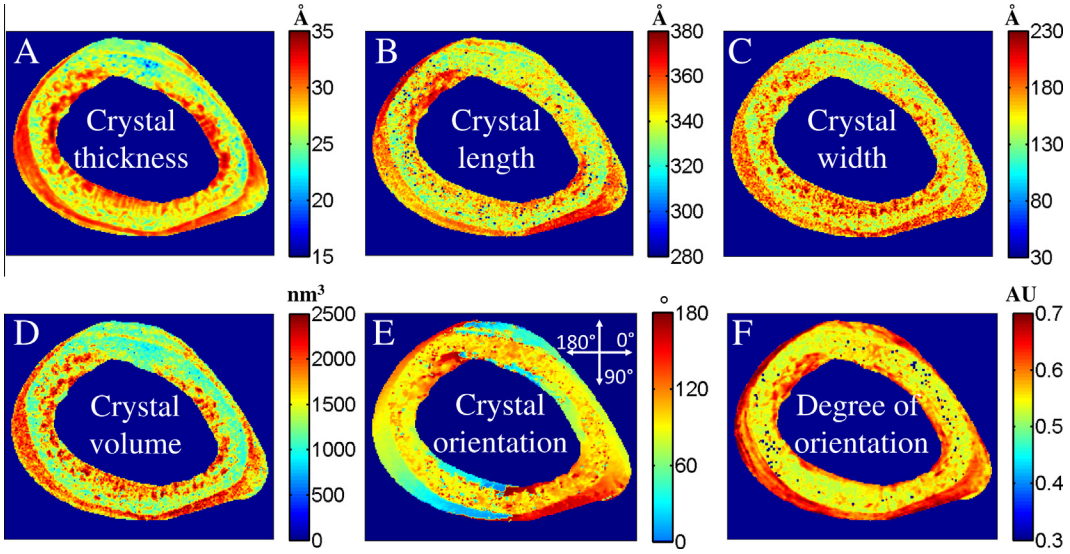

Fig. 3. SAXS and WAXS parameter maps of a healthy mature rat femoral cortex. Mineral plate thickness (SAXS) (A) and crystal length ([002] WAXS) (B), crystal width ([310] WAXS) (C), and the crystal volume (SAXS & WAXS) (D) maps are presented. Moreover, the predominant orientation (E) and degree of orientation (F) (SAXS) maps are also shown. Orientation angles in (E) are indicated (note that the angles range from 0° to 180°, thus all vertical orientations are 90°). The layered structure between periosteal, central, and endosteal regions is obvious at all sub-images. Also small islands with larger sized crystals are present inside the central cortex. This is consistent with findings by others of remnants of calcified cartilage islands inside the rat cortex (Bach-Gansmo et al., 2013).

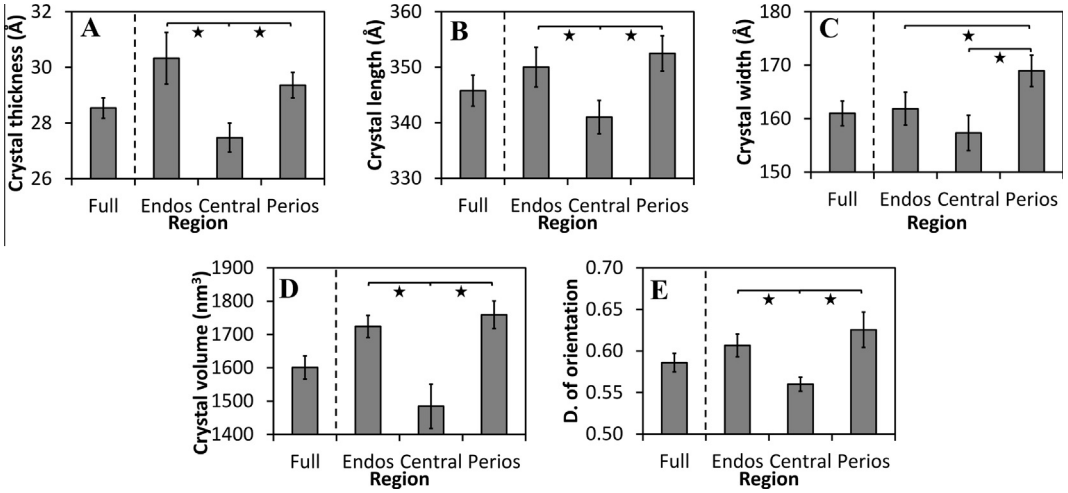

Fig. 4. Average crystal dimensions (A–D) and degree of orientations (E) in whole cortex (Full), endosteal (Endos), central (Central), and periosteal (Perios) regions of cortex of mature (healthy and OVX) samples. Significance for Mann-Whitney *U*-test are indicated $^{*}p < 0.05$.

should not be mixed with the main orientation of the crystals which is along the long axis of the bone.

In mature samples, crystal dimensions were generally higher in the endosteal and periosteal regions than in the central region (Fig. 4A–D). Crystal thickness (Fig. 4A), crystal length (Fig. 4B), crystal volume (Fig. 4D), and degree of orientation (Fig. 4E) were significantly higher in endosteal and periosteal regions compared to central region ($p < 0.05$). Crystal width (Fig. 4C) was significantly higher in periosteal region compared to central and endosteal regions ($p < 0.05$).

When averages for the endosteal, central and periosteal areas of all samples were collected, significant correlations between the crystal size and organization related parameters were found. Degree of orientation correlated significantly with crystal length ($R^2 = 0.84$, $p < 0.01$), crystal volume ($R^2 = 0.51$, $p < 0.01$), crystal width ($R^2 = 0.41$, $p < 0.05$), and crystal thickness ($R^2 = 0.37$, $p < 0.05$). As expected, crystal thickness, crystal length and crystal width all correlated highly with crystal volume ($R^2 > 0.70$, $p < 0.01$). These results were in line with the point-by-point correlations where crystal volume correlated significantly with all the dimensions, while crystal thickness remained as the most important factor ($R^2 = 0.73$, $p < 0.001$, Fig. 6). In FTIR data, increase in XLR correlated significantly with the decrease in APS ($R^2 = 0.59$, $p < 0.01$) and with increase in crystallinity ($R^2 = 0.61$, $p < 0.001$).

Due to the small number of samples, the young, mature healthy, and mature OVX samples were compared only qualitatively. However crystal dimensions were clearly lower in the young sample compared to the mature samples (Fig. 5A–D). No clear differences were observed in degree of orientation (Fig. 5E). Descriptively, mineral/matrix ratio was lower in OVX samples than in young and mature healthy samples (Fig. 5F) whereas collagen maturity (Fig. 5G) was lower in young sample than in mature samples. Acid phosphate substitution (Fig. 5H) was higher in young and OVX samples than in mature healthy samples.

4. Discussion

In the present study, mineralization across rat femoral cortex was studied using high resolution scanning SAXS, WAXS, and FTIR microspectroscopy. We found that the mineral crystal sizes were larger in endosteal and periosteal surfaces of bone compared to the central region of the cortex. Further, the predominant orientation followed the edge of the cortex while it was more randomly distributed in the central region. These findings indicate a higher and more organized degree of mineralization in the regions where the later formed lamellar bone is present (Weiner and Traub, 1992; Weiner et al., 1991). On the other hand, in the central region (oldest bone) the mineral crystals were smaller and they were more

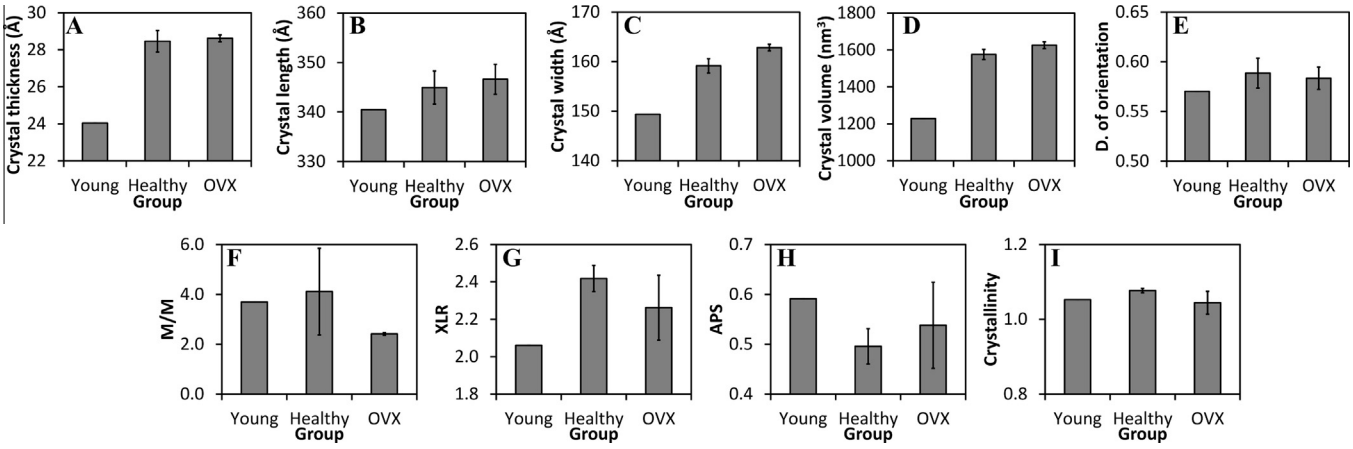

Fig. 5. Average crystal dimensions (A–D), degree of orientations (E), and mineral/matrix ratio (F), collagen maturity (G), acid phosphate substitution (H), and crystallinity (I) in whole cortex in young (Young), mature healthy (Healthy), and mature OVX (OVX) samples.

randomly oriented, presumably because of the quick formation during endochondral ossification that occurred during the original mineralization of the long bone (Bach-Gansmo et al., 2015, 2013; Shipov et al., 2013). Moreover, the collection of point-by-point SAXS and WAXS data together with biochemical composition, enabled us to determine spatial distribution of the mineral crystal volume, not previously reported.

SAXS has been widely used to determine the mineral plate thickness in bone. Especially a method proposed by Fratzl et al. has been used extensively (Bunger et al., 2006; Fratzl et al., 1991, 1996a,b; Rinnerthaler et al., 1999). However, this model requires specific assumptions for mineral phase fraction which may not be valid in all cases, *e.g.*, in newly formed bone or when comparing bone with different turnover rate. This method also uses only the high-q data (q = 1–2 Å^{-1}) which generally have larger uncertainties. Therefore, Bunger et al. (2010) proposed a curve fitting method, adopted in the current study. This model includes no assumption on the mineral phase fraction, however, there may be uncertainties due to correlations of some of the fitting parameters (Kaspersen et al., 2016). The thickness is mainly determined by the Guinier region of the data, *i.e.*, the region where the fitting is performed (Fig. 1). However, when polydispersity and concentration effects are present, the Guinier region will be influenced by both the thickness, the polydispersity, and the structure factor effects due to the high volume fraction of mineral plates in bone (Kaspersen et al., 2016). As the thickness and polydispersity correlate to some extent, the polydispersity was kept fixed at 0.3 during the optimizations to assure comparable results between the fits. The present study contains fits of several thousand datasets, and the fact that the values are similar within each region, but different between periosteal, central, and endosteal regions, serves as a validation of the fit parameters. The model has previously been used to study the effect of OVX-induced osteoporosis in trabecular bone (Mathavan et al., 2015), effects of $SrCl_2$ treatment on OVX-rat cortical bone (Bunger et al., 2010), and newly formed callus tissue (Turunen et al., 2014). WAXS has been used to study the other crystal dimensions, *i.e.*, length and width, in bone. However, simultaneous SAXS and WAXS measurement are rare (Acerbo et al., 2014; Daniels et al., 2010; Giannini et al., 2014; Paris, 2008; Sandholzer et al., 2014). In two studies only a partial coverage of the azimuthal angles has been used (Acerbo et al., 2014; Daniels et al., 2010), which might result in reduced detection of the orientational features. In another study the main focus was on orientational properties (Giannini et al., 2014) without determining the dimensions of the crystals. To our knowledge, this is the first study where combined high resolution scanning SAXS and WAXS are used to study mineralization across the bone cortex cross-section.

Rat long bones are initially formed by rapid endochondral ossification. As a result of bone growth and maturation, lamellar bone is formed in the periosteal and endosteal regions (newer bone) and the remnants of the initial mineralization form the central region (older bone) (Bach-Gansmo et al., 2015, 2013; Shipov et al., 2013; Weiner and Traub, 1992). In addition to the different regions, also small islands inside the central region are visible in SAXS/WAXS parameter maps (Fig. 3). The mineral crystals are clearly larger in these islands compared to the other central region. This is consistent with a previous study by Bach-Gansmo et al. (2013), which identified these islands as being calcified cartilage and showed that they have a higher calcium content compared to the surrounding tissue. The effect of maturation is visible from the relative areas of these regions (Fig. 2B). The central region represents a higher proportion of the cross-section in the young bone (69%) than in the healthy mature (53%) and OVX (58%) samples. Despite being based on very low number of samples, this is consistent with previous findings (Bach-Gansmo et al., 2013; Danielsen et al., 1993). Compared to regions of bone formation in mechanically loaded and non-loaded rat ulna imaged after labeling (Fig. 1 in (Noble et al., 2003), Fig. 6 in (Robling et al., 2006), and Fig. 1B in (Checa et al., 2015)), the present SAXS and WAXS parameter maps show a similar pattern (Fig. 3), *i.e.*, in the periosteal (but also endosteal) regions of the bone. The strains due to mechanical loading are more prominent especially on the periosteal regions, and based on finite element models, the fluid velocities have been calculated to be higher at both periosteal and endosteal regions (Pereira et al., 2015). Load-induced fluid flow has been proposed to provide the mechanism for mechano-coupling (Klein-Nulend et al., 1995). This may serve as one explanation for the apparent increased remodeling activity and bone adaptations leading to growth of the mineral crystals also on the nanoscale. Indeed, the contour plots of fluid velocities in Fig. 9 in Pereira et al. (2015) match distinctly the layered structure observed in this study (Fig. 3).

The predominant orientation of the mineral crystals followed the edge of the cortex whereas it was more random in the central region. However, the orientation determined in 2-dimensions may be restrictive. In case of bone, the predominant orientation of the collagen fibers, and mineral crystals, is mainly in the direction of loading. In long bones, *e.g.*, the femur, the main loading directions are along the bone shaft, which is perpendicular to the 2-dimensional cross-sections and parallel to the X-ray beam used in this study. Thus, the predominant orientation in this case is the mineral crystal orientation in the studied plane. For comprehensive evaluation of the 3-dimensional orientation, the data has to be collected in different sample angles. Such techniques are currently being developed for SAXS for sectioned (Georgiadis et al., 2015) and 3D specimens (Liebi et al., 2015; Schaff et al., 2015).

Differences between the young, mature healthy, and mature OVX samples were observed. In younger rat bone, the mineral crystal dimensions were generally lower than in the mature rats (Fig. 4). Although statistical comparison between the groups was not possible due to low number of samples, the results are in line with previous studies; mineral crystals have been shown to be larger in OVX rats compared to control (Mathavan et al., 2015). FTIR analyses revealed, as expected, that the crystallinity and the amount of mature cross-links (XLR) were lower in younger bone, as compared to mature rat bone, whereas acid phosphate substitution (APS), an indicator of new bone formation, was higher in young than in mature bone. The ability to use these techniques for monitoring the tissues for both mineral and collagen maturity was also evident in the inverse correlation between APS and XLR

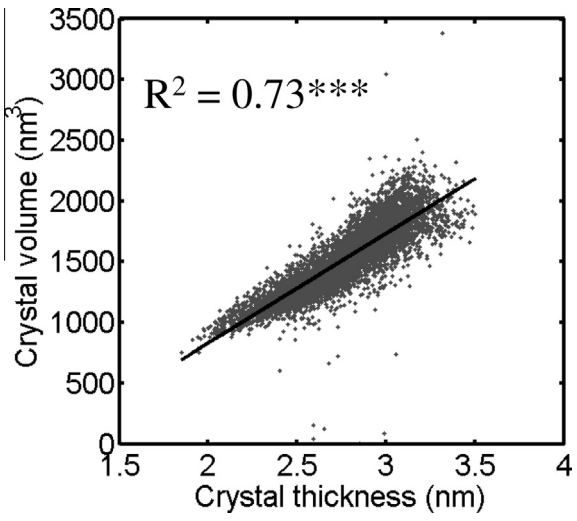

Fig. 6. Point-by-point correlation between mineral crystal thickness and crystal volume using data points from all down scaled (factor of 4) data-maps. Pearson correlation was significant $p < 0.001$.

and linear correlation between XLR and crystallinity. APS is higher when bone formation is present (Miller et al., 2001; Roberts et al., 1992) whereas XLR and crystallinity increase during tissue aging (Paschalis et al., 2001, 1996; Turunen et al., 2012, 2011). Based on the present results, the sizes of the mineral crystals in control and osteoporotic rats 18 weeks after ovariectomy, were similar.

A strong correlation between the mineral crystal volume and crystal thickness, crystal length and crystal width were found. This is expected, since the volume is a product of the dimensions. The strength of the correlations is in line with the scales of the dimensions. Since the crystal thickness is relatively much smaller than the length and width (5–15%), even small changes in the thickness result in a large change in the volume. Thus, mineral crystal volume, or at least the spatial variation of it, can be evaluated indirectly from the mineral crystal thickness, even when WAXS and the information about the crystal length and width are not available.

The major limitation of the present study is the low number of samples, which impedes the statistical power for the interpretation of the differences between the samples and the different regions of cortex. However, this is partly counteracted by the high level of data collection with small X-ray spot-size. Therefore, the focus was on studying the behavior across the cortex where over 16,000 measurement points are available per sample.

5. Conclusions

In this study, novel analysis methods were used to probe the differences of molecular composition and nanostructure across rat bone cortex in young, and mature healthy and mature OVX rat samples. Furthermore, combined point-by-point SAXS and WAXS data collection enabled the quantification of the spatial variation of crystal volume across rat bone cortex. Mineral crystal size was found to be significantly lower in the central region, which seems to be remnants from the early and rapidly formed bone during endochondral ossification (Bach-Gansmo et al., 2015, 2013; Shipov et al., 2013), compared to the newer formed and more lamellar structured bone at the endosteal and periosteal regions.

Disclosures

The authors have no conflicts of interest.

Acknowledgements

Funding from Swedish Foundation for Strategic Research, Academy of Finland (project 286091), Kuopio University Hospital (VTR project 5041741, PY210) and the strategic funding of University of Eastern Finland. The authors would like to acknowledge the MAX-IV laboratory, Lund, Sweden for providing the beamtime at the D7 beamline, as well as the European Community's Seventh Framework Programme (FP7/2007-2013) under grant agreement no. 262348 (ESMI, European Soft Matter Infrastructure network), which provided beamtime at the cSAXS beamline of the SLS at the Paul Scherrer Institut, Villigen, Switzerland. We want to thank Mea Pelkonen for help with sample preparation. FS would like to thank the TUM Graduate School.

References

Acerbo, A.S., Kwaczala, A.T., Yang, L., Judex, S., Miller, L.M., 2014. Alterations in collagen and mineral nanostructure observed in osteoporosis and pharmaceutical treatments using simultaneous small- and wide-angle X-ray scattering. Calcif. Tissue Int. 95, 446–456. http://dx.doi.org/10.1007/s00223-014-9913-0.

Bach-Gansmo, F.L., Irvine, S.C., Bruel, A., Thomsen, J.S., Birkedal, H., 2013. Calcified cartilage islands in rat cortical bone. Calcif. Tissue Int. 92, 330–338. http://dx.doi.org/10.1007/s00223-012-9682-6.

Bach-Gansmo, F.L., Weaver, J.C., Jensen, M.H., Leemreize, H., Mader, K.S., Stampanoni, M., Brüel, A., Thomsen, J.S., Birkedal, H., 2015. Osteocyte lacunar properties in rat cortical bone: differences between lamellar and central bone. J. Struct. Biol. 191, 59–67. http://dx.doi.org/10.1016/j.jsb.2015.05.005.

Bagi, C.M., Wilkie, D., Georgelos, K., Williams, D., Bertolini, D., 1997. Morphological and structural characteristics of the proximal femur in human and rat. Bone 21, 261–267, doi: S875632829700121X [pii].

Boskey, A., Pleshko Camacho, N., 2007. FT-IR imaging of native and tissue-engineered bone and cartilage. Biomaterials 28, 2465–2478. http://dx.doi.org/10.1016/j.biomaterials.2006.11.043.

Bunger, M.H., Foss, M., Erlacher, K., Li, H., Zou, X., Langdahl, B.L., Bunger, C., Birkedal, H., Besenbacher, F., Pedersen, J.S., Bünger, M.H., Bünger, C., 2006. Bone nanostructure near titanium and porous tantalum implants studied by scanning small angle X-ray scattering. Eur. Cell. Mater. 12, 81–91.

Bunger, M.H., Oxlund, H., Hansen, T.K., Sorensen, S., Bibby, B.M., Thomsen, J.S., Langdahl, B.L., Besenbacher, F., Pedersen, J.S., Birkedal, H., Bünger, M.H., Sørensen, S., 2010. Strontium and bone nanostructure in normal and ovariectomized rats investigated by scanning small-angle X-ray scattering. Calcif. Tissue Int. 86, 294–306. http://dx.doi.org/10.1007/s00223-010-9341-8.

Bunk, O., Bech, M., Jensen, T.H., Feidenhans'l, R., Binderup, T., Menzel, A., Pfeiffer, F., 2009. Multimodal X-ray scatter imaging. New J. Phys. 11. http://dx.doi.org/10.1088/1367-2630/11/12/12301.

Camacho, N.P., Rinnerthaler, S., Paschalis, E.P., Mendelsohn, R., Boskey, A.L., Fratzl, P., 1999. Complementary information on bone ultrastructure from scanning small angle X-ray scattering and Fourier-transform infrared microspectroscopy. Bone 25, 287–293. http://dx.doi.org/10.1016/S8756-3282(99)00165-9.

Checa, S., Hesse, B., Roschger, P., Aido, M., Duda, G.N., Raum, K., Willie, B.M., 2015. Skeletal maturation substantially affects elastic tissue properties in the endosteal and periosteal regions of loaded mice tibiae. Acta Biomater. 21, 154–164. http://dx.doi.org/10.1016/j.actbio.2015.04.020.

Courtland, H.-W., Nasser, P., Goldstone, A.B., Spevak, L., Boskey, A.L., Jepsen, K.J., 2008. Fourier transform infrared imaging microspectroscopy and tissue-level mechanical testing reveal intraspecies variation in mouse bone mineral and matrix composition. Calcif. Tissue Int. 83, 342–353. http://dx.doi.org/10.1007/s00223-008-9176-8.

Daniels, J.E., Pontoni, D., Hoo, R.P., Honkimäki, V., 2010. Simultaneous small-and wide-angle scattering at high X-ray energies. J. Synchrotron Radiat. 17, 473–478. http://dx.doi.org/10.1107/S0909049510016456.

Danielsen, C.C., Mosekilde, L., Svenstrup, B., 1993. Cortical bone mass, composition, and mechanical properties in female rats in relation to age, long-term ovariectomy, and estrogen substitution. Calcif. Tissue Int. 52, 26–33.

Donnelly, E., Chen, D.X., Boskey, A.L., Baker, S.P., Van Der Meulen, M.C.H., 2010. Contribution of mineral to bone structural behavior and tissue mechanical properties. Calcif. Tissue Int. 87, 450–460. http://dx.doi.org/10.1007/s00223-010-9404-x.

Durchschlag, E., Paschalis, E.P., Zoehrer, R., Roschger, P., Fratzl, P., Recker, R., Phipps, R., Klaushofer, K., 2006. Bone material properties in trabecular bone from human iliac crest biopsies after 3- and 5-year treatment with risedronate. J. Bone Miner. Res. 21, 1581–1590. http://dx.doi.org/10.1359/jbmr.060701.

Fratzl, P., Fratzl-Zelman, N., Klaushofer, K., Vogl, G., Koller, K., 1991. Nucleation and growth of mineral crystals in bone studied by small-angle X-ray scattering. Calcif. Tissue Int. 48, 407–413.

Fratzl, P., Groschner, M., Vogl, G., Plenk Jr, H., Eschberger, J., Fratzl-Zelman, N., Koller, K., Klaushofer, K., 1992. Mineral crystals in calcified tissues: a comparative study by SAXS. J. Bone Miner. Res. 7, 329–334. http://dx.doi.org/10.1002/jbmr.5650070313.

Fratzl, P., Schreiber, S., Klaushofer, K., 1996a. Bone mineralization as studied by small-angle X-ray scattering. Connect. Tissue Res. 34, 247–254. http://dx.doi.org/10.3109/03008209609005268.

Fratzl, P., Schreiber, S., Roschger, P., Lafage, M.H., Rodan, G., Klaushofer, K., 1996b. Effects of sodium fluoride and alendronate on the bone mineral in minipigs: a small-angle X-ray scattering and backscattered electron imaging study. J. Bone Miner. Res. 11, 248–253. http://dx.doi.org/10.1002/jbmr.5650110214.

Gadeleta, S.J., Boskey, A.L., Paschalis, E., Carlson, C., Menschik, F., Baldini, T., Peterson, M., Rimnac, C.M., 2000. A physical, chemical, and mechanical study of lumbar vertebrae from normal, ovariectomized, and nandrolone decanoate-treated cynomolgus monkeys (*Macaca fascicularis*). Bone 27, 541–550. http://dx.doi.org/10.1016/S8756-3282(00)00362-8.

Georgiadis, M., Guizar-Sicairos, M., Zwahlen, A., Trüssel, A.J., Bunk, O., Müller, R., Schneider, P., 2015. 3D scanning SAXS: a novel method for the assessment of bone ultrastructure orientation. Bone 71, 42–52. http://dx.doi.org/10.1016/j.bone.2014.10.002.

Giannini, C., Siliqi, D., Ladisa, M., Altamura, D., Diaz, A., Beraudi, A., Sibillano, T., De Caro, L., Stea, S., Baruffaldi, F., Bunk, O., 2014. Scanning SAXS–WAXS microscopy on osteoarthritis-affected bone – an age-related study. J. Appl. Crystallogr. 47, 110–117. http://dx.doi.org/10.1107/S1600576713030215.

Glatter, O., Kratky, O., 1982. Small Angle X-Ray Scattering. Academic Press, London.

Henrich, B., Bergamaschi, A., Broennimann, C., Dinapoli, R., Eikenberry, E.F., Johnson, I., Kobas, M., Kraft, P., Mozzanica, A., Schmitt, B., 2009. PILATUS: a single photon counting pixel detector for X-ray applications. Nucl. Instrum. Methods Phys. Res. Sect. A 607, 247–249. http://dx.doi.org/10.1016/j.nima.2009.03.200.

Isaksson, H., Turunen, M.J., Rieppo, L., Saarakkala, S., Tamminen, I.S., Rieppo, J., Kröger, H., Jurvelin, J.S., 2010. Infrared spectroscopy indicates altered bone turnover and remodeling activity in renal osteodystrophy. J. Bone Miner. Res. 25, 1360–1366. http://dx.doi.org/10.1002/jbmr.10.

Kalu, D.N., 1991. The ovariectomized rat model of postmenopausal bone loss. Bone Miner. 15, 175–191. http://dx.doi.org/10.1016/0169-6009(91)90124-I.

Kaspersen, J.D., Turunen, M.J., Mathavan, N., Lages, S., Pedersen, J.S., Olsson, U., Isaksson, H., 2016. Small-Angle X-Ray Scattering Demonstrates Similar Nanostructure in Cortical Bone From Young Adult Animals of Different Species. Calcif. Tissue Int. 99, 76–87. http://dx.doi.org/10.1007/s00223-016-0120-z.

Klein-Nulend, J., van der Plas, A., Semeins, C.M., Ajubi, N.E., Frangos, J.A., Nijweide, P. J., Burger, E.H., 1995. Sensitivity of osteocytes to biomechanical stress in vitro. FASEB J. 9, 441–445.

Landis, W.J., Hodgens, K.J., Song, M.J., Arena, J., Kiyonaga, S., Marko, M., Owen, C., McEwen, B.F., 1996. Mineralization of collagen may occur on fibril surfaces: evidence from conventional and high-voltage electron microscopy and three-dimensional imaging. J. Struct. Biol. 117, 24–35. http://dx.doi.org/10.1006/jsbi.1996.0066.

Lange, C., Li, C., Manjubala, I., Wagermaier, W., Kühnisch, J., Kolanczyk, M., Mundlos, S., Knaus, P., Fratzl, P., 2011. Fetal and postnatal mouse bone tissue contains more calcium than is present in hydroxyapatite. J. Struct. Biol. 176, 159–167. http://dx.doi.org/10.1016/j.jsb.2011.08.003.

Liebi, M., Georgiadis, M., Menzel, A., Schneider, P., Kohlbrecher, J., Bunk, O., Guizar-Sicairos, M., 2015. Nanostructure surveys of macroscopic specimens by small-angle scattering tensor tomography. Nature 527, 349–352. http://dx.doi.org/10.1038/nature16056.

Marcott, C., Reeder, R.C., Paschalis, E.P., Tatakis, D.N., Boskey, A.L., Mendelsohn, R., 1998. Infrared microspectroscopic imaging of biomineralized tissues using a mercury-cadmium-telluride focal-plane array detector. Cell. Mol. Biol. (Noisy-le-grand) 44, 109–115.

Mathavan, N., Turunen, M.J., Tägil, M., Isaksson, H., 2015. Characterising bone material composition and structure in the ovariectomized (OVX) rat model of osteoporosis. Calcif. Tissue Int. 97, 134–144. http://dx.doi.org/10.1007/s00223-015-9991-7.

Miller, L.M., Vairavamurthy, V., Chance, M.R., Mendelsohn, R., Paschalis, E.P., Betts, F., Boskey, A.L., 2001. In situ analysis of mineral content and crystallinity in bone using infrared micro-spectroscopy of the nu(4) PO(4)(3−) vibration. Biochim. Biophys. Acta 1527, 11–19.

Noble, B.S., Peet, N., Stevens, H.Y., Brabbs, A., Mosley, J.R., Reilly, G.C., Reeve, J., Skerry, T.M., Lanyon, L.E., 2003. Mechanical loading: biphasic osteocyte survival and targeting of osteoclasts for bone destruction in rat cortical bone. Am. J. Physiol. Cell Physiol. 284, C934–C943. http://dx.doi.org/10.1152/ajpcell.00234.2002.

Paris, O., 2008. From diffraction to imaging: new avenues in studying hierarchical biological tissues with X-ray microbeams (Review). In: Biointerphases 3, FB16. http://dx.doi.org/10.1116/1.2955443.

Paschalis, E.P., DiCarlo, E., Betts, F., Sherman, P., Mendelsohn, R., Boskey, A.L., 1996. FTIR microspectroscopic analysis of human osteonal bone. Calcif. Tissue Int. 59, 480–487.

Paschalis, E.P., Verdelis, K., Doty, S.B., Boskey, A.L., Mendelsohn, R., Yamauchi, M., 2001. Spectroscopic characterization of collagen cross-links in bone. J. Bone Miner. Res. 16, 1821–1828. http://dx.doi.org/10.1359/jbmr.2001.16.10.1821.

Pauw, B.R., 2014. Corrigendum: everything SAXS: small-angle scattering pattern collection and correction (2013 J. Phys.: Condens. Matter 25 383201). J. Phys. Condens. Matter 26, 239501. http://dx.doi.org/10.1088/0953-8984/26/23/239501.

Pereira, A.F., Javaheri, B., Pitsillides, A.A., Shefelbine, S.J., 2015. Predicting cortical bone adaptation to axial loading in the mouse tibia. J. R. Soc. Interface 12, 1–14. http://dx.doi.org/10.1098/rsif.2015.0590.

Rieppo, J., Hyttinen, M.M., Jurvelin, J.S., Helminen, H.J., 2004. Reference sample method reduces the error caused by variable cryosection thickness in Fourier transform infrared imaging. Appl. Spectrosc. 58, 137–140. http://dx.doi.org/10.1366/000370204322729577.

Rinnerthaler, S., Roschger, P., Jakob, H., Nader, A., Klaushofer, K., Fratzl, P., 1999. Scanning small angle X-ray scattering analysis of human bone sections. Calcif. Tissue Int. 64, 422–429. http://dx.doi.org/10.1007/PL00005824.

Roberts, J.E., Bonar, L.C., Griffin, R.G., Glimcher, M.J., 1992. Characterization of very young mineral phases of bone by solid state 31 phosphorus magic angle sample spinning nuclear magnetic resonance and X-ray diffraction. Calcif. Tissue Int. 50, 42–48.

Robling, A.G., Castillo, A.B., Turner, C.H., 2006. Biomechanical and molecular regulation of bone remodeling. Annu. Rev. Biomed. Eng. 8, 455–498. http://dx.doi.org/10.1146/annurev.bioeng.8.061505.095721.

Sandholzer, M.A., Sui, T., Korsunsky, A.M., Damien Walmsley, A., Lumley, P.J., Landini, G., 2014. X-ray scattering evaluation of ultrastructural changes in human dental tissues with thermal treatment. J. Forensic Sci. 59, 769–774. http://dx.doi.org/10.1111/1556-4029.12400.

Schaff, F., Bech, M., Zaslansky, P., Jud, C., Liebi, M., Guizar-Sicairos, M., Pfeiffer, F., 2015. Six-dimensional real and reciprocal space small-angle X-ray scattering tomography. Nature 527, 353–356. http://dx.doi.org/10.1038/nature16060.

Schwarcz, H.P., McNally, E.A., Botton, G.A., 2014. Dark-field transmission electron microscopy of cortical bone reveals details of extrafibrillar crystals. J. Struct. Biol. 188, 240–248. http://dx.doi.org/10.1016/j.jsb.2014.10.005.

Shimada, T., Doi, M., Okano, K., 1988. Concentration fluctuation of stiff polymers. I. Static structure factor. J. Chem. Phys. 88, 2815. http://dx.doi.org/10.1063/1.454016.

Shipov, A., Zaslansky, P., Riesemeier, H., Segev, G., Atkins, A., Shahar, R., 2013. Unremodeled endochondral bone is a major architectural component of the cortical bone of the rat (*Rattus norvegicus*). J. Struct. Biol. 183, 132–140. http://dx.doi.org/10.1016/j.jsb.2013.04.010.

Spevak, L., Flach, C.R., Hunter, T., Mendelsohn, R., Boskey, A., 2013. Fourier transform infrared spectroscopic imaging parameters describing acid phosphate substitution in biologic hydroxyapatite. Calcif. Tissue Int. 92, 418–428. http://dx.doi.org/10.1007/s00223-013-9695-9.

Turunen, M.J., Saarakkala, S., Rieppo, L., Helminen, H.J., Jurvelin, J.S., Isaksson, H., 2011. Comparison between infrared and Raman spectroscopic analysis of maturing rabbit cortical bone. Appl. Spectrosc. 65, 595–603. http://dx.doi.org/10.1366/10-06193.

Turunen, M.J., Saarakkala, S., Helminen, H.J., Jurvelin, J.S., Isaksson, H., 2012. Age-related changes in organization and content of the collagen matrix in rabbit cortical bone. J. Orthop. Res. 30, 435–442. http://dx.doi.org/10.1002/jor.21538.

Turunen, M.J., Lages, S., Labrador, A., Olsson, U., Tägil, M., Jurvelin, J.S., Isaksson, H., 2014. Evaluation of composition and mineral structure of callus tissue in rat femoral fracture. J. Biomed. Opt. 19, 025003. http://dx.doi.org/10.1117/1.JBO.19.2.025003.

Weiner, S., Traub, W., 1992. Bone structure: from angstroms to microns. FASEB J. 6, 879–885.

Weiner, S., Arad, T., Traub, W., 1991. Crystal organization in rat bone lamellae. FEBS Lett. 285, 49–54. http://dx.doi.org/10.1016/0014-5793(91)80722-F.